JOURNAL OF SPACECRAFT AND ROCKETS
Vol. 32, No. 4, July–August 1995

Titan IV Motor Failure and Redesign Analyses

I-Shih Chang,* N. R. Patel,† and S. Yang‡
The Aerospace Corporation, El Segundo, California 90245

A fully interactive, gas-flow–grain structural analysis was developed and applied to reconstruct the failure mode of the first prequalification motor and to evaluate the redesigned grain configuration for the Titan IV solid-rocket-motor upgrade. The gas-flow analysis was based on an adaptive, unstructured, finite-element method for the solution of full Navier–Stokes flows inside solid-rocket-motors. The grain structural analysis was conducted using a general-purpose, finite-element program with the consideration of viscoelastic properties of the propellant and orthotropic properties of the graphite-epoxy motor case. The exact deformed grain geometry was considered in the fully interactive, gas-flow–grain structural analysis. Results of the analyses for the first prequalification motor and for the redesign motor agreed well with the data obtained from the static firing tests. The study provided confirmation and confidence required for the implementation of the grain modification. The qualification program for the Titan IV solid-rocket-motor upgrade was completed with five successful tests of the motors with the redesigned grain configuration.

Nomenclature

c_p = specific heat at constant pressure, Btu/lb-°R
$\mathbf{D}$ = conservative variable vector in Eq. (1)
E = Young's modulus in Eq. (2)
$\mathbf{E}_r$ = r-direction flux vector in Eq. (1)
$\mathbf{E}_x$ = x-direction flux vector in Eq. (1)
$\mathbf{F}$ = Flux vector in Eq. (1)
f_i = ith component of external loading vector
G = shear modulus, $E/2(1+\nu)$
p = gas pressure, psi
Pr = gas Prandtl number
r = radial coordinate from motor centerline, in.
s = propellant burn rate, in./s
T = temperature, °R
t = time, s
u_i = ith component of grain displacement vector
x = axial coordinate, in.
z_i = ith component of a position vector
α = coefficient of thermal expansion
γ = ratio of gas specific heats
δ = geometry index in Eq. (1) ($\delta = 0$ for plane two-dimensional flow; $\delta = 1$ for axisymmetry)
ε = first strain invariant
θ = temperature difference, $T - T_0$, °R
μ = gas viscosity (lbf-s/in.^{2})
ν = Poisson's ratio

Subscripts

c = motor chamber condition
0 = initial condition

Introduction

THE U.S. Air Force Titan IV solid-rocket-motor upgrade,[1] shown in Fig. 1, is being developed to launch large payloads. The program suffered a temporary setback when a static firing test of the first prequalification motor (PQM-1) failed at 1.58 s after ignition.[2] The evaluation of test data from the motor firing suggested that the large pressure gradient on the unchamfered aft-segment propellant grain resulted in an excessive grain deformation, which, in turn, increased pressure on the propellant grain as illustrated in Fig. 2. This coupling of the gas pressure and grain deformation continued until the propellant grain cracked at the stress-relief groove and deformed excessively to constrict the gas flow at the forward end of the aft segment. This caused a corresponding rise of the head-end pressure until the motor case ruptured.

To confirm and reconstruct the postulated failure mode for the SRMU PQM-1, a novel, multidisciplinary interactive analysis method shown in Fig. 3 was developed. This analysis method combines the disciplines of propulsion, gasdynamics, and structural mechanics and provides a means to evaluate the detailed gas flowfield and exact propellant-grain structural response during a solid-rocket-motor firing. A unique feature of this analysis methodology is the gas-flow analysis, which solved the full Navier–Stokes equations for viscous, compressible, axisymmetric flows inside an arbitrary computational domain prescribed by the ablated motor and nozzle insulation and receding propellant burnback boundary. This paper documents the results of the fully interactive gas-flow–grain structural analyses performed during the mishap investigation and during the redesign evaluation of the Titan IV solid-motor upgrade.

Background

The Titan IV solid-rocket-motor upgrade is 10.5 ft in diameter and 112.4 ft long; it consists of three segments made of filament-wound graphite-epoxy composites and joined together by steel clevis rings. A composite of IM7 graphite fibers and HBRF-55A epoxy resin is employed for the forward dome and cylindrical segment, the cylindrical center segment, and the cylindrical portion of the aft segment, which is mated with the steel aft dome. In addition to the filament windings, the segment joint regions are reinforced with unidirectional tapes consisting of IM7 graphite fibers preimpregnated with 3501-6 epoxy resin. The motor case is thermally protected from combustion gas by Kevlar-loaded ethylenepropylenediene monomer wound elastomeric insulation in the major portion of the cylindrical region of the segments. Premolded silica-loaded, ethylenepropylenediene monomer insulation is used for the thermal protection of the forward dome, the steel clevis rings, and the aft dome. The motor is loaded with 688,850 lb of hydroxylterminated polybutadiene solid propellant (69% ammonium perchlorate +19% aluminum +12% binder) and weighs about 772,750 lb. The propellant has a star-shaped grain in the forward segment and a tapered cylindrical grain in the center and aft segments. A stress-relief groove is molded in the center and in the aft segment, as shown in Fig. 1, to minimize the stress concentration at the bondline between the propellant and the motor case insulation. The connection between the aft composite segment and the steel dome, as well as the connection between composite segments and steel clevis rings,

Received Nov. 15, 1993; revision received June 20, 1994; accepted for publication June 20, 1994.

*Distinguished Engineer, Vehicle Performance Subdivision. Member AIAA.
†Senior Engineering Specialist, Structural Mechanics Subdivision.
‡Member of Technical Staff, Vehicle Performance Subdivision.

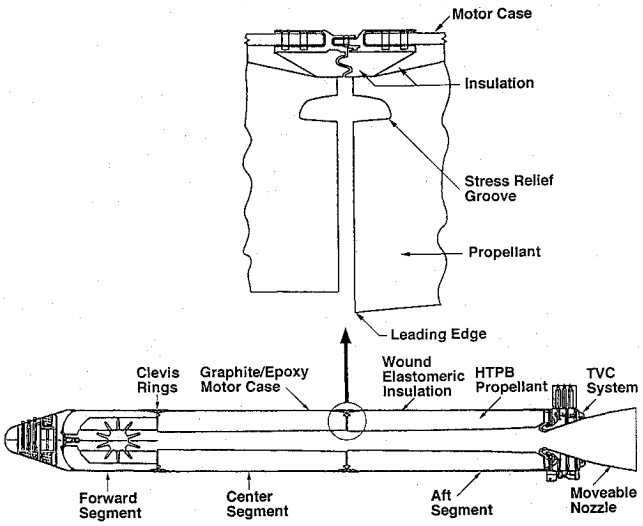

Fig. 1 Titan IV SRMU motor assembly (PQM-1).

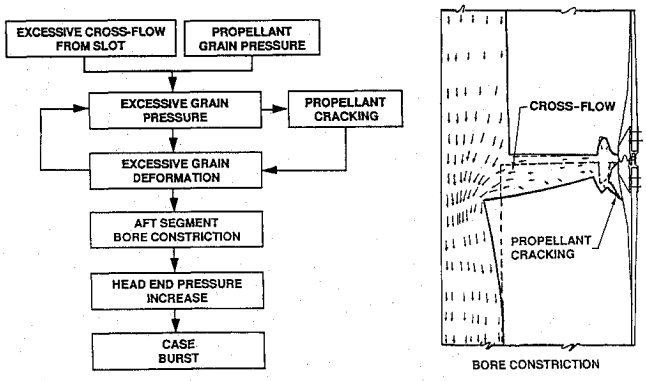

Fig. 2 SRMU PQM-1 test failure scenario.

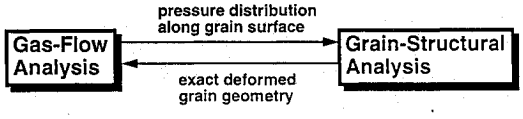

- Solution of full Navier-Stokes equations with viscous effects
- Adaptive, unstructured, automatic finite-element mesh generation
- Arbitrary motor chamber and nozzle with receding propellant burn-back geometry
- ABAQUS general purpose finite-element analysis program
- Visco-elastic property for propellant grain
- Orthotropic property for graphite/epoxy motor case

Fig. 3 Fully interactive gas-flow–grain structural analysis simulation.

is accomplished by factory joints using two staggered rows of 120 1.125-in.-diam steel pins. The motor is assembled with two field joints located between the forward and center segments and between the center and aft segments. Each field joint has a single row of 144 equally spaced 1.125-in.-diam steel pins. A thrust-vector control system with a flexseal assembly provides the nozzle with a maximum 6-deg gimbaling capability. The Titan IV launch vehicle with two strap-on solid-rocket-motor upgrades is designed to provide a 25% increase in the payload delivery capability over that of the current Titan IV vehicle with steel motor cases. The Titan IV is the most powerful solid rocket motor in the U.S. Air Force space launch program.

Following the failure of the first prequalification motor, a mishap investigation team acted to identify the cause of the test failure.[3] A fault tree was constructed to ensure proper evaluation of every potential cause of the test failure, which included items such as test facilities and the design and manufacture of all motor components. Each item of the fault tree was carefully examined and scrutinized. The cause of the failure was identified to be the result of gas-flow–grain structural interaction, which led to the excessive deformation of the propellant grain and constriction of the gas flow inside the motor chamber.

A fully interactive gas-flow–grain structural analysis was developed and applied to reconstruct the failure mode of the motor. In this analysis approach, the pressure distribution along the propellant-grain surface was obtained from the gas-flow analysis and used in the grain structural analysis at the initial time. The combustion gas-pressure load resulted in propellant-grain deformation, which in turn induced the change in gas-pressure distribution inside the motor. The exact deformed grain geometry generated from the grain structural analysis then was fed back to the gas-flow analysis for a continued, interactive solution at the next time. This process was able to provide analysis results that closely matched with the test data from the first motor firing. Although a one-dimensional model for gas-flow–grain structural interaction was discussed[4] for a motor of simple geometry, the detailed gas-flow–grain structural interactive analysis with the consideration of the exact deformed grain geometry presented is required for the failure-mode reconstruction, and for the redesign evaluation of the Titan IV motor with a complicated interior configuration. As a part of the PQM-1 recovery program, the propellant grain at the leading edge of the center and aft segments was chamfered to reduce the pressure gradient on the grain surface and to eliminate the recurrence of the PQM-1 failure. The fully interactive gas-flow–grain structural analysis also was utilized to evaluate the redesigned grain configuration. The study provides the analysis support to the qualification program of the Titan IV solid-rocket-motor upgrade.

Internal Flow Analysis

An efficient method[5] for the solution of compressible viscous flows inside solid rocket motors was used to provide timely flow analysis support for the mishap investigation and for the redesign evaluation of the SRMU. The method applied an adaptive, unstructured, finite-element mesh generation technique and a cell-centered, second-order flux correction transport scheme for the solution of full Navier–Stokes equations, which included every term in the viscous stress tensor in an axisymmetric or two-dimensional flow:

$$\frac{\partial \mathbf{D}}{\partial t} + \frac{\partial \mathbf{E}_x}{\partial x} + \frac{\partial \left(r^{\delta} \mathbf{E}_r\right)}{r^{\delta}\, \partial r} + \frac{\delta \mathbf{F}}{r} = 0 \qquad (1)$$

The method, which was applied in Ref. 6 to the study of a plane two-dimensional, supersonic flow over a circular cylinder, was extended and streamlined in Ref. 4 for the solution of axisymmetric flows inside solid rocket motors of any arbitrary configuration with a nonuniform inlet boundary condition. This method also had been extended to a multimaterial transient heat-conduction analysis in Ref. 7. With a known initial motor interior configuration, the method allowed the computational boundaries, including propellant burnbacks, ablated motor case insulation, and eroded nozzle and exit-cone surfaces at any time after ignition, to be determined intelligently. The method is flexible and versatile in treating the complicated geometry in multidimensional space and is especially suited for the internal flow analysis of the SRMU with ablated motor and nozzle insulation and receding propellant burnback boundary.

The computational domain in this study covered the full length of the SRMU interior configuration. This included the forward segment, the center segment, the aft segment, the submerged nozzle, and a portion of the exit cone. The three-dimensional star-shaped grain in the forward segment was approximated in an axisymmetric analysis by a cylindrical grain with an equivalent hydraulic diameter equal to 4 times the cross-sectional area divided by the wetted perimeter at each axial station at every time slice. The mass flow rate from the cylindrical grain surface was adjusted to be equal to that from the star-shaped grain on the forward segment at each axial station at every time slice. The inlet boundary lay on the propellant burning surface, and the flow variables on the inlet boundary were determined from propellant burn rate, chamber temperature, and chamber pressure. At each integration step, the gas pressure on the propellant burning surface was recomputed from the energy

Table 1 Lamina properties[a]

Ply type	Modulus, 10^6 psi						Poisson's ratio		
	E_{11}	E_{22}	E_{33}	G_{12}	G_{13}	G_{23}	ν_{12}	ν_{13}	ν_{23}
Hoop Winding	22.0	0.262	0.262	0.45	0.1	0.1	0.272	0.311	0.311
Helical Winding	20.9	0.262	0.262	0.45	0.1	0.1	0.272	0.311	0.311
Broadgood	20.6	1.23	1.23	0.723	0.469	0.469	0.275	0.313	0.313

[a]Subscript 1 denotes fiber direction, 2 normal-to-fiber direction (in-plane), and 3 cross-ply direction.

equation, using an average of presently and previously computed gas densities. The newly computed pressure was used to provide a new gas density from the equation of state on the inlet boundary for the next integration step. For the viscous flow analysis, the nozzle and exit-cone wall constituted a nonslip boundary with a specified wall temperature. The exit plane was set at a location 20 in. downstream of the nozzle throat. This insured that no subsonic pocket existed near the exit plane, and any numerical error resulting from linear extrapolation near the exit plane would not propagate back and affect the upstream results. The initial guess for the quasisteady flow calculation at each time slice was based on a one-dimensional, isentropic assumption.

The flowfield associated with the deformed grain inside the PQM-1 could not be analyzed easily with other existing methods, mainly because of the difficulty in modeling the exact configuration of the deformed grain. Further difficulty arose when excessive grain radial deflection made the bore radius at the leading edge of the aft-segment propellant grain smaller than the geometric throat of the nozzle. This produced another sonic flow at the leading edge of the deformed aft-segment grain, in addition to the one at the geometric throat of the nozzle. The adaptive, unstructured, finite-element method used in this study considered the exact deformed grain geometry and encountered no difficulty in obtaining the solution for the complicated flow situation inside the PQM-1 motor. The quasisteady analysis implied that the flow attained steady state at each time slice. The difference in the mass flow rate generated on the propellant burning surface and that passed through the nozzle throat at each time slice produced the measurable effect of time rate of change of the chamber pressure, dp/dt. The propellant burn rate is a function of pressure and is set to $s = 0.0677p^{0.232}$. The gas properties used in the analysis are

$$\gamma = 1.13, \qquad c_p = 0.587\,\text{Btu/lb-°R}$$

$$T_c = 6400°\text{R}, \qquad Pr = 0.57$$

$$\mu = \mu_c(T/T_c)^{0.67} \qquad \text{with} \quad \mu_c = 0.1382 \times 10^{-7}\,\text{lbf-s/in.}^2$$

Grain Structural Analysis

The structural analysis portion of the interactive analysis was based on the following generalized equations of displacement:

$$\Delta^2 u_i + \frac{1}{1-2\nu}\frac{\partial \varepsilon}{\partial z_i} = -\frac{f_i}{G} + \frac{2(1+\nu)}{1-2\nu}\alpha\frac{\partial \theta}{\partial z_i} \tag{2}$$

The discretized finite-element equations were solved by the ABAQUS computer program[8] using the linear elastic element option. This program is known to provide accurate results for a nearly incompressible material such as the propellant. Since the data obtained from the motor firing test indicated that the forward-segment grain deformation did not significantly affect the gas flow, the structural analysis effort was focused on the center and aft segments. Because of the large size of the analysis model, the two segments were analyzed separately for the thermal, gravitational, and pressure loads. The structural model included the composite motor case, polymeric insulation, and propellant grain. The eight-noded, axisymmetric solid elements were used to represent the graphite-epoxy motor case, rubber insulation, and solid propellant in the finite-element analysis. Each element of the motor case was provided with a set of orthotropic material properties summarized in Table 1. A special type of hybrid element, which contains both stress and displacement in the formulation of the element and is suitable for nearly incompressible materials, was used for the rubber insulation and solid propellant. The viscoelastic properties of these materials were taken into account in a linear-elastic analysis by varying their moduli as a function of motor burn time.

Table 2 Insulation and propellant properties

Material	Modulus, psi		Poisson's ratio	Thermal expansion coefficient, 10^{-6} (in./in.)/°F
	Ignition	Storage		
Insulation (EPDM)	8040	2000	0.499	8.5
Insulation (WEI)	2570	570	0.4994	8.5
Propellant:				
60°F	1200	230	0.499985	4.6
90°F	900	155	0.499985	4.6

During the initial phase of the anomaly investigation, the propellant modulus was not well defined, because the initial motor-propellant mechanical properties were not fully characterized. Based on the preliminary data[9] from the propellant uniaxial tension tests at various loading rates, a propellant ignition modulus ranging from 900 to 3000 psi was considered in the fully interactive gas-flow–grain structural analysis. The radial deflection for the high-modulus (stiff) propellant was not large enough to cause the observed chamber pressure drop from the head end to the aft end of the motor. On the other hand, too much deformation of the low-modulus (soft) propellant would produce a higher pressure drop from the head end to the aft end of the motor than that observed in the test. The "correct" modulus derived from the analysis for the PQM-1 propellant at 60°F was found to vary from 1200 psi at ignition to 1040 psi at 1.58 s into motor burn. This time-dependent propellant modulus produced a very good match between the computed and the measured pressures inside the motor chamber during the 1.58-s motor firing of the PQM-1. Incidentally, the propellant ignition modulus was verified by the propellant mechanical property test[10] and subscale pressurization test,[11] after the anomaly analysis described in this paper had been completed. The properties for the insulation and propellant used in this analysis are summarized in Table 2.

Test Data and Results of Analysis

PQM-1 Anomaly

The test motor was provided with static pressure probes near the ignitor housing at the head end of the motor and at the joint between the aft dome and the nozzle assembly. Shown in Fig. 4 is the motor-chamber pressure history obtained during the PQM-1 firing. The measured data showed that the difference between the head end and aft end pressure deviated significantly from that of the prefire prediction for a well-behaved motor. During a normal motor firing, one would expect that, after the ignition transient period (0.2 s) had passed, the difference between the head end and the aft-end pressure would decrease with time as propellant receded. In this case, however, the difference continued to rise after the ignition transient period had passed. The head-end pressure not only exceeded the predicted maximum value of 1170 psi at 0.4 s, but continued to rise to 1835 psi, when the motor case ruptured.

To help identify the cause of this abnormal pressure response of the motor, the motor-case hoop growth measured during test firing was examined. The test motor was instrumented with hoop wire gages at the locations indicated in Fig. 5, which also shows the motor hoop strain measurements at 0.4, 1.4, and 1.58 s into motor

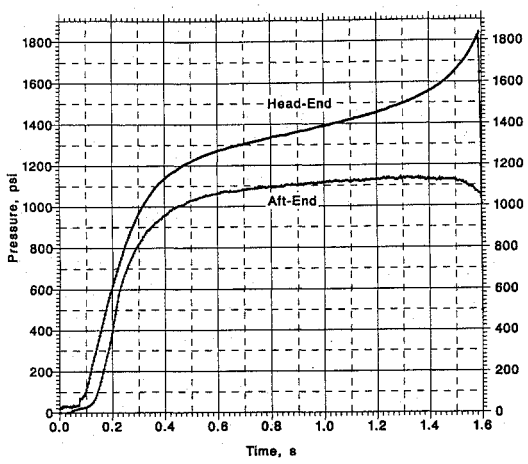

Fig. 4 Measured head-end and aft-end pressure histories.

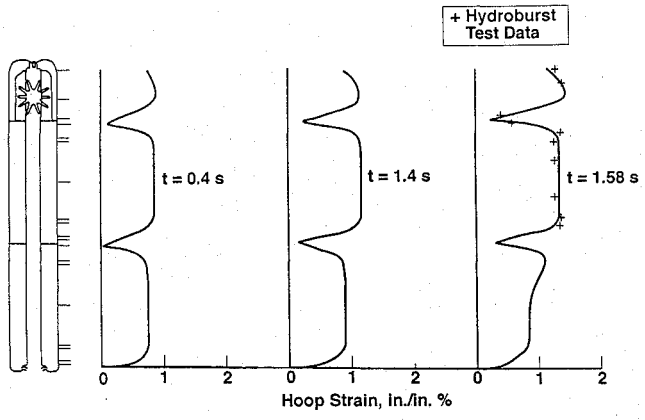

Fig. 5 Motor-case hoop-strain measurements.

firing. At 0.4 s, the hoop-strain response of all three segments was not significantly different. At later times, however, the forward and center segments bulged out distinct further than the aft segment. At the time of failure, the chamber pressure downstream of the joint between the center and aft segments was much smaller than the pressure in both the forward and center segment, suggesting a flow constriction between center and aft segment. The measured head-end pressure at 1.58 s reached the burst strength of the motor case. Full-scale hydroburst tests conducted during the motor case development program demonstrated a burst strength ranging from 1730 to 1830 psi. Based on the hydroburst test data, rupture of the PQM-1 test motor case at 1835 psi was to be expected. The excellent agreement of the hoop-wire measurements with the hydroburst test data confirmed that the motor case behaved normally from the structural perspective.

The gas flowfields were obtained at nine times, namely 0.2, 0.4, 0.7, 1.0, 1.2, 1.4, 1.5, 1.55, and 1.58 s after PQM-1 ignition. At each time, the adaptive, unstructured finite-element mesh for the gas-flow analysis was generated automatically for the computational domain prescribed by the recessed and deformed propellant surface and ablated nozzle and exit-cone wall boundaries. The number of elements in the computational domain ranged from 4333 to 4465 for the PQM-1. Figure 6 illustrates the unstructured grid with deformed grain geometry used in the flowfield calculation for the PQM-1 at 1.58 s. The required computation time for a converged solution of the full Navier–Stokes equations at each time slice was 2 h on a Cray X-MP/18 supercomputer.

Figure 7 depicts the finite-element models for the grain structural analysis of the center and the aft segment. There were 13,010 nodes and 4207 elements for the center segment, and 11,618 nodes and 3557 elements for the aft segment. After the propellant was cast into segments, the propellant shrank because of cooldown from the curing temperature of 135°F. In addition, the propellant deformed further under its own weight. The center- and aft-segment grain

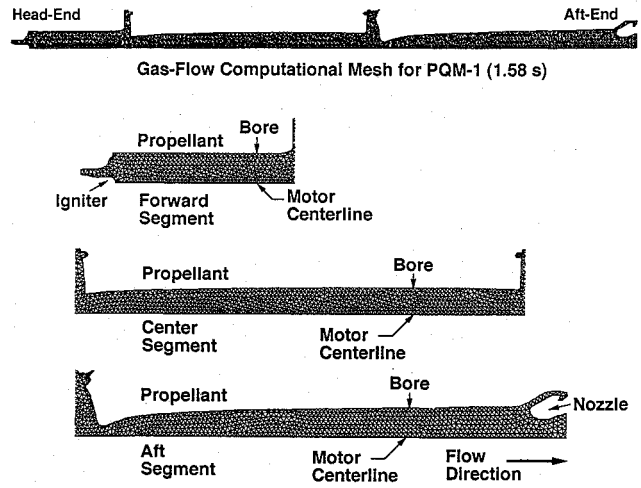

Fig. 6 Finite-element mesh for gas-flow analysis.

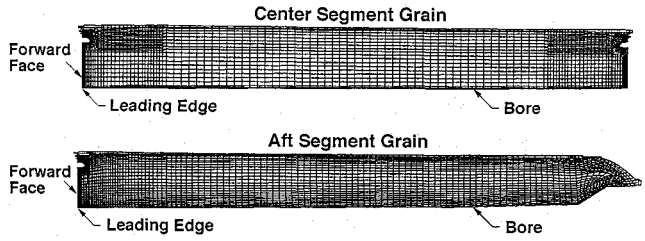

Fig. 7 Finite-element models for grain structural analysis.

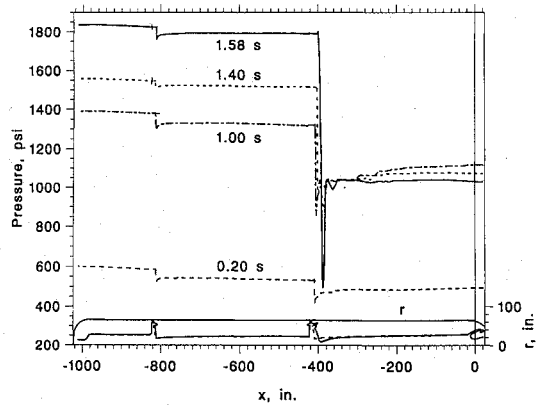

Fig. 8 Pressure distributions on the grain surface.

deformations due to thermal cooldown and slump were determined by the structural analysis, and the deformed grain geometry was used as the initial condition for the gas-flow analysis. The grain structural analysis also was conducted at the same times as those of the gas-flow analysis.

Figure 8 shows the computed pressure distributions on the grain surface at 0.2, 0.4, 1.2, and 1.58 s into motor firing. The deformed grain geometry at 1.58 s from ignition, as predicted by the grain structural analysis and used in calculating the pressure acting on the grain, is shown in the bottom portion of the figure. The pressure difference between the forward and the center segment was fairly steady with time. On the other hand, the pressure difference between the center and aft segment increased dramatically with time, because of an increased rate of the grain deformation. At 1.58 s, this pressure difference exceeded 600 psi. Figure 9 shows the Mach-number distribution at the motor centerline for the same four times. For the viscous flow analysis, the gas velocity on the grain surface was determined from the propellant burning rate. The Mach number on the grain surface was very small, about 0.003. However, the Mach number at the motor centerline just downstream of the forward face of the deformed aft segment grain reached 1.0 at 1.58 s.

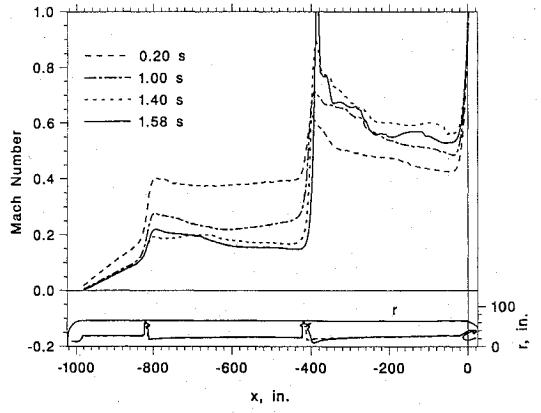

Fig. 9 Mach-number distributions on the motor centerline.

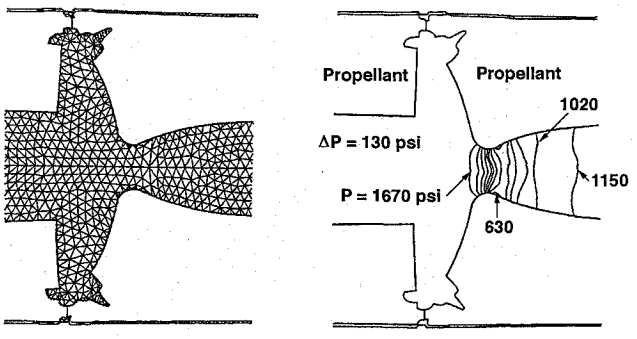

Fig. 10 Computed and measured chamber pressure histories.

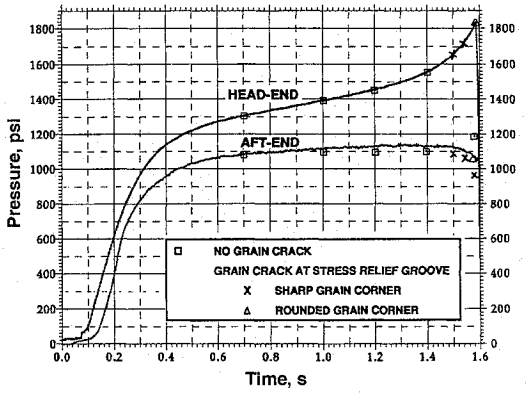

Fig. 11 Gas-pressure contour near the flow constriction area.

The chamber pressure histories obtained from the gas-flow analysis at the head end and at the aft end of the motor are compared with those obtained from the motor test in Fig. 10. The gas-flow analysis incorporated additional grain deformations and burn surfaces caused by the cracking of the aft-segment propellant stress-relief groove starting from 1.5 s after motor ignition. The cracking of the groove was deduced from the grain structural analysis, as the computed strain at the propellant stress relief groove exceeded the maximum allowable strain. The good agreement between the computed and the measured pressure history is evident from Fig. 10. The results of the gas-flow analysis indicated that the deformed grain constricted the gas flow at the joint between the center and the aft segment and caused a corresponding rise of the head-end pressure, until the motor case ruptured at 1.58 s after motor ignition. This is shown in the enlarged pressure contour plot near the flow constriction area on the forward face of the aft segment in Fig. 11.

The grain deformation of the aft segment at 1.4 s is shown in Fig. 12. The leading-edge deformation history of both the center and aft segments is shown in Fig. 13. The radial displacement of the center segment remained almost constant with time, whereas the aft-segment displacement continued to increase with time until it constricted the gas flow. The membrane hoop strain predicted for

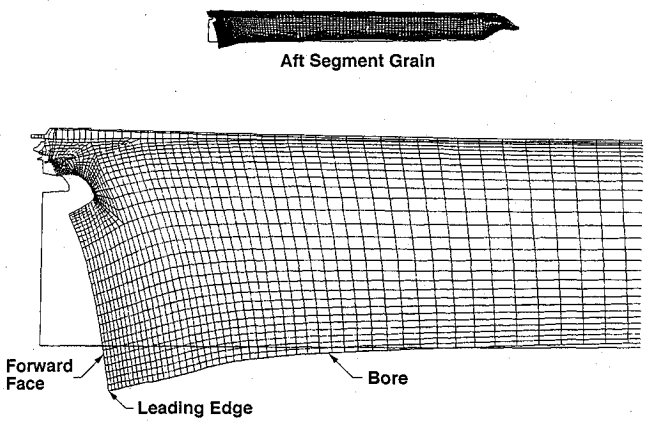

Fig. 12 Grain deformation of the aft segment.

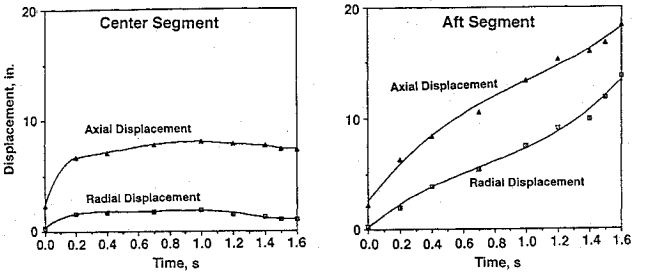

Fig. 13 Leading-edge deformation histories.

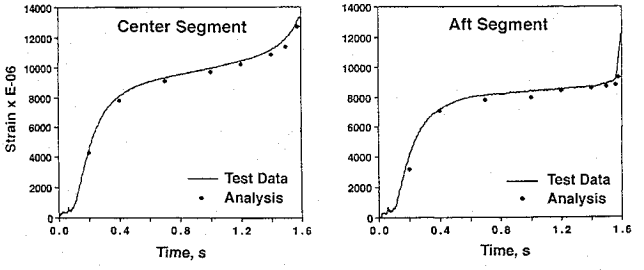

Fig. 14 Computed and measured hoop-strain histories.

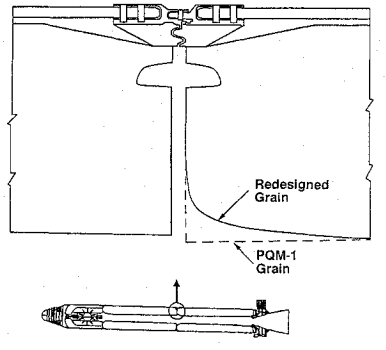

Fig. 15 Comparison of PQM-1 grain and redesigned grain configuration.

the center and aft segments is compared in Fig. 14 with the measured data. The comparison shows good correlation, which further validates the predicted pressure distribution on the grain surfaces. The knowledge gained from the confirmation and reconstruction of the failure mode paved the way for further evaluation of the redesign configuration.

Corrective Action

An obvious fix for the motor was to reduce excessive grain deformations and to eliminate the flow constriction in the motor center bore. This was accomplished through recontouring and chamfering the forward corner of the propellant grain for both the center and aft segments as shown in Fig. 15. For the redesigned motor,

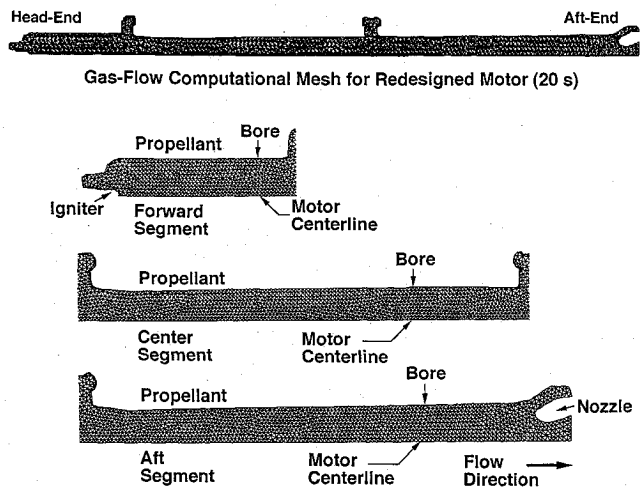

Fig. 16 Finite-element mesh for gas-flow analysis (redesign).

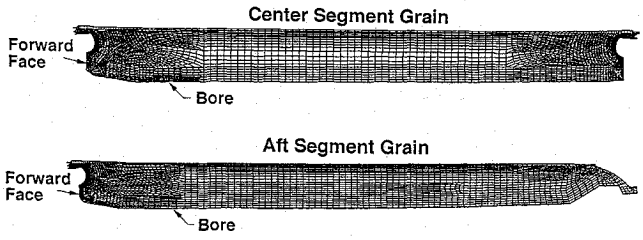

Fig. 17 Finite-element models for grain structural analysis (redesign).

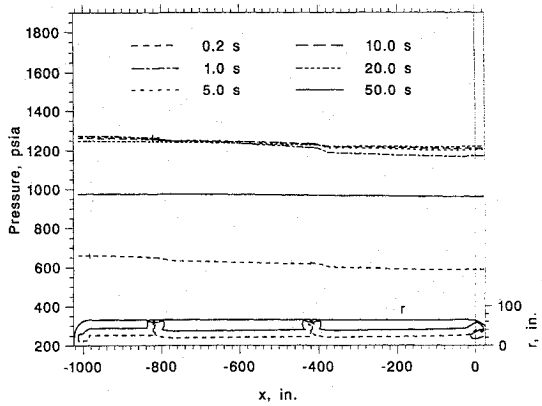

Fig. 18 Pressure distributions on the grain surface (redesign).

the fully interactive analysis was carried out at 11 times, namely 0.2, 0.4, 0.7, 1, 2, 5, 10, 20, 30, 40, and 50 s after motor ignition. The number of elements in the flow analysis domain ranged from 5148 to 6592. Figure 16 shows the computation grid for the flowfield calculation at 20 s. The corresponding finite-element models for the center- and aft-segment grain structural analysis are shown in Fig. 17. There were 22,014 nodes and 7215 elements for the center segment, and 14,744 nodes and 4817 elements for the aft segment in the grain structural analysis. The worst-case condition associated with the propellant ignition modulus of 900 psi corresponding to the propellant mean bulk temperature of 90°F was studied. Figures 18 and 19 show the pressure and Mach-number distributions inside the motor at six times. The deformed grain configurations at 0.2 and 50 s also are given in the bottom portions of the figures.

The pressure history inside the chamber (Fig. 20) was very close to that computed from SPP[12] for a simple one-dimensional flow, because the crossflow effect was insignificant inside the motor with the chamfered grain. The computed pressure drops between the segment joints for the first motor and for the redesigned grains are compared in Fig. 21. For the chamfered grain, the analysis predicted

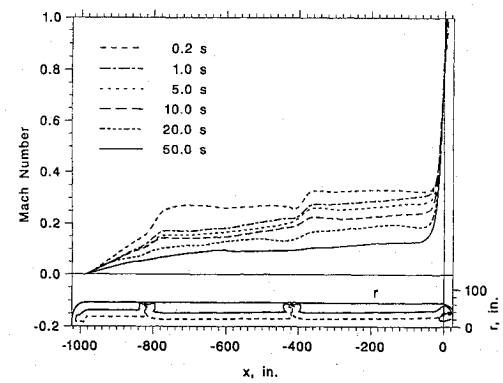

Fig. 19 Mach-number distributions on the redesigned motor centerline.

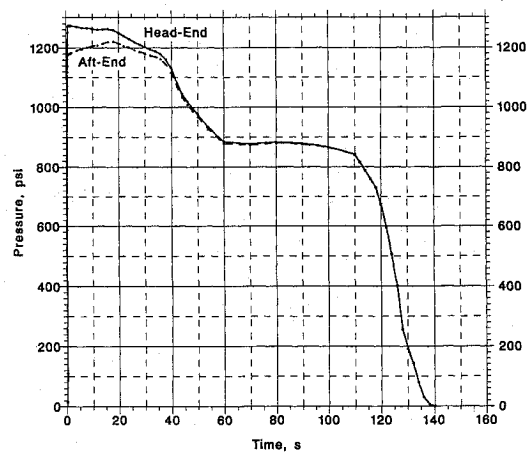

Fig. 20 Head-end and aft-end pressure histories for the redesigned motor.

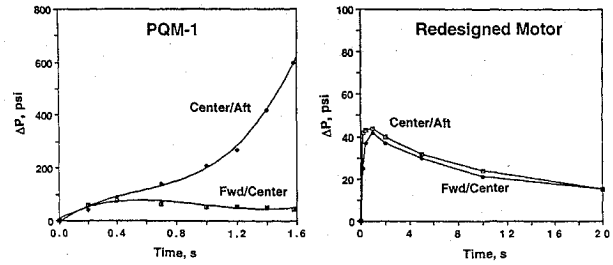

Fig. 21 Computed pressure drop between the segment joints.

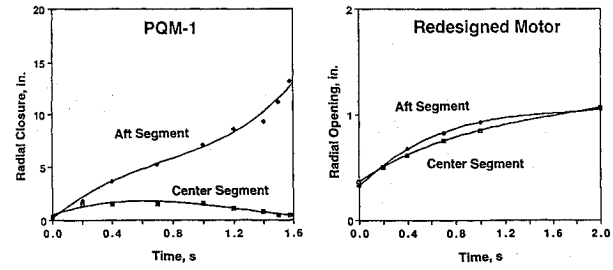

Fig. 22 Radial deformation histories of the grain leading edge.

a maximum pressure drop of 45 psi at 1.0 s, which decreased to 20 psi at 20 s after ignition. This pressure drop was much smaller than 600 psi, which led to the failure of the first test motor. The Mach number was predicted to remain below 0.35 inside the motor throughout the motor firing.

Figure 22 shows the comparison of the radial deformation obtained from the analyses for the PQM-1 and the redesigned grain. The excessive radial closure of up to 13 in. at the forward leading edge of the PQM-1 aft segment was eliminated with the

redesigned grain. The analysis further showed radial openings for both the center and aft segments with the redesigned grain geometry, thereby completely eliminating constriction of the gas flow inside the motor. The study essentially confirmed the adequacy of the new SRMU grain design for ground test and eventual implementation in flight motors. Since the cracking of the propellant stress-relief groove was identified as the secondary cause of the prequalification motor failure, an improved propellant stress-relief groove[13] was incorporated into the motor to provide a significant improvement in the grain structural margin of safety. Subsequently, five static firing tests of the motors with the reconfigured grain geometry were conducted successfully. To prevent recurrence of a similar anomaly in the solid-rocket-motor development program, a new policy[14] was adopted. The policy requires that a multidimensional interactive gas-flow–grain structural analysis be implemented for a new or redesigned segmented or monolithic solid rocket motor with full or partial cylindrical perforated grain.

Conclusions

This paper documents the results of a fully interactive gas-flow–grain structural analysis and compares them with the motor test data. The analysis developed in this study considered the exact deformed grain geometry, propellant burnback configuration, and submerged, ablated nozzle contour; it served to reconstruct the failure mode of the first firing and to evaluate the grain redesign for the Titan IV solid-rocket-motor upgrade. The study confirmed the adequacy of the new grain design. Five motors with the redesigned grain configuration were fired successfully in the motor qualification program.

Acknowledgments

This work was supported by the U.S. Air Force Space and Missile Systems Center under Contract F04701-88-C-0089. The authors wish to thank N. N. Au, former General Manager of the Vehicle and Control Systems Division, The Aerospace Corporation, for his guidance and many valuable suggestions during the course of this study. The authors also wish to thank Y. S. Pan and S. N. Sallam for their many valuable contributions to the grain structural analysis, and S. M. Johnson for her outstanding effort in preparing the manuscript for publication.

References

[1]Anon., "Titan IV SRMU Preliminary Design Review," Hercules, Inc., Magna, UT, Feb. 1989.

[2]Spark, J. H., "Titan IV Solid-Rocket-Motor Upgrade (SRMU) PQM-1 Full Scale Static Firing Report," Hercules, Inc., SDRL Item SR-T05-002, Magna, UT, Sept. 1991.

[3]Anders, W. H., "Titan IV SRMU PQM-1 Static Firing Test Failure Investigation," Final Report. to Lt. Gen. E. P. Barry, AFSSD, Los Angeles AFB, June 1991.

[4]Glick, R. L., Caveny, L. H., and Thurman J. L., "Internal Ballistics of Slotted-Tube, Solid-Propellant Rocket Motors," *Journal of Spacecraft and Rockets*, Vol. 4, No. 4, 1967, pp. 525–530.

[5]Chang, I-S., "An Efficient, Intelligent Solution for Viscous Flows inside Solid Rocket Motors," Applied Physics Lab., JANNAF, Paper 2D-1, *CPIA-PUB-560*, Vol. 2, p. 47, Laurel, MD, Oct. 1990; also AIAA Paper 91-2429, June 1991.

[6]Thareja, R. R., Stewart, J. R., Hassan, O., Morgan K., and Peraire J., "A Point Implicit Unstructured Grid Solver for the Euler and Navier–Stokes Equations," AIAA Paper 88-0036, Jan. 1988.

[7]Chang, I-S., "Adaptive, Unstructured, Finite-Element, Multi-material, Thermal Analysis," *Journal of Spacecraft and Rockets*, Vol. 30, No. 1, 1993, pp. 43–50.

[8]Anon., *ABAQUS Theory Manual*, Hibbitt, Karlsson & Sorensen, Inc., Providence, RI, Aug. 1982.

[9]Bohney-Lang, J., "Mechanical Characterization of QDT Propellant and Case Bond Characterization," Hercules Inc., Report HITC/T660/84-2577, Magna, UT, June 1990.

[10]Bohney-Lang, J., "Specific Data Report, Titan IV SRMU PQM-1 Recovery Propellant and Case Bond Subscale Testing," Hercules Inc., Report BU90U-2000-1023, Magna, UT, May 1992.

[11]Christensen, L., and Purcell, S., "Determination of the Effective Modulus for a Solid Propellant Grain during Ignition Pressurization," AIAA Paper 92-3824, July 1992.

[12]Nickerson, G. R., Dunn, S. S., and Berker, D. R., "The Solid Propellant Rocket Motor Performance Computer Program (SPP) Version 7.0," Edwards AFB, AFAL-TR-87-078, Edwards Air Force Base, CA, Feb. 1992.

[13]Chang, I-S., "Propellant Stress Relief Groove for the Titan IV Solid Rocket Motor Upgrade," *Journal of Spacecraft and Rockets*, Vol. 31, No. 2, 1994, pp. 285–289.

[14]"Multi-dimensional Interactive Gas-Flow/Grain Structural Analysis for Solid Rocket Motors," Commander's Policies, Air Force Space and Missile Systems Center, SMC Regulation 800-19, Los Angeles, Air Force Base, CA, April 1993.

E. A. Thornton
Associate Editor